



**HAL**  
open science

# Surface slip and off-fault deformation patterns in the 2013 M W 7.7 Balochistan, Pakistan earthquake: Implications for controls on the distribution of near-surface coseismic slip

Robert Zinke, James Hollingsworth, James Dolan

► **To cite this version:**

Robert Zinke, James Hollingsworth, James Dolan. Surface slip and off-fault deformation patterns in the 2013 M W 7.7 Balochistan, Pakistan earthquake: Implications for controls on the distribution of near-surface coseismic slip. *Geochemistry, Geophysics, Geosystems*, 2014, 15 (12), pp.5034-5050. 10.1002/2014gc005538 . hal-02196084

**HAL Id: hal-02196084**

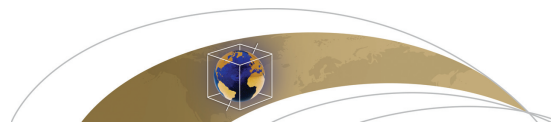
**<https://hal.science/hal-02196084v1>**

Submitted on 18 Mar 2022

**HAL** is a multi-disciplinary open access archive for the deposit and dissemination of scientific research documents, whether they are published or not. The documents may come from teaching and research institutions in France or abroad, or from public or private research centers.

L'archive ouverte pluridisciplinaire **HAL**, est destinée au dépôt et à la diffusion de documents scientifiques de niveau recherche, publiés ou non, émanant des établissements d'enseignement et de recherche français ou étrangers, des laboratoires publics ou privés.

Copyright



## RESEARCH ARTICLE

10.1002/2014GC005538

## Key Points:

- Half of surface rupture in 2013 Balochistan occurred as off-fault deformation
- Type and thickness of geologic materials control distribution of surface strain
- Off-fault deformation has implications for slip rates material behavior and hazard

## Supporting Information:

- Readme
- Tables S1–S3
- Figure S1

## Correspondence to:

R. W. Zinke,  
rzinke@usc.edu

## Citation:

Zinke, R., J. Hollingsworth, and J. F. Dolan (2014), Surface slip and off-fault deformation patterns in the 2013  $M_w$  7.7 Balochistan, Pakistan earthquake: Implications for controls on the distribution of near-surface coseismic slip, *Geochem. Geophys. Geosyst.*, 15, 5034–5050, doi:10.1002/2014GC005538.

Received 12 AUG 2014

Accepted 21 NOV 2014

Accepted article online 4 DEC 2014

Published online 30 DEC 2014

## Surface slip and off-fault deformation patterns in the 2013 $M_w$ 7.7 Balochistan, Pakistan earthquake: Implications for controls on the distribution of near-surface coseismic slip

Robert Zinke<sup>1</sup>, James Hollingsworth<sup>2,3</sup>, and James F. Dolan<sup>1</sup>

<sup>1</sup>Department of Earth Sciences, University of Southern California, Los Angeles, California, USA, <sup>2</sup>Géoazur, University of Nice Sophia-Antipolis, CNRS, Observatoire de la Côte d'Azur, Valbonne, Nice, France, <sup>3</sup>Now at Arup, London, UK

**Abstract** Comparison of 398 fault offsets measured by visual analysis of WorldView high-resolution satellite imagery with deformation maps produced by COSI-Corr subpixel image correlation of Landsat-8 and SPOT5 imagery reveals significant complexity and distributed deformation along the 2013  $M_w$  7.7 Balochistan, Pakistan earthquake. Average slip along the main trace of the fault was 4.2 m, with local maximum offsets up to 11.4 m. Comparison of slip measured from offset geomorphic features, which record localized slip along the main strand of the fault, to the total displacement across the entire width of the surface deformation zone from COSI-Corr reveals ~45% off-fault deformation. While previous studies have shown that the structural maturity of the fault exerts a primary control on the total percentage of off-fault surface deformation, large along-strike variations in the percentage of strain localization observed in the 2013 rupture imply the influence of important secondary controls. One such possible secondary control is the type of near-surface material through which the rupture propagated. We therefore compared the percentage off-fault deformation to the type of material (bedrock, old alluvium, and young alluvium) at the surface and the distance of the fault to the nearest bedrock outcrop (a proxy for sediment thickness along this hybrid strike slip/reverse slip fault). We find significantly more off-fault deformation in younger and/or thicker sediments. Accounting for and predicting such off-fault deformation patterns has important implications for the interpretation of geologic slip rates, especially for their use in probabilistic seismic hazard assessments, the behavior of near-surface materials during coseismic deformation, and the future development of microzonation protocols for the built environment.

### 1. Introduction

Numerous recent studies of large historical surface ruptures indicate significant variations in the percentage of off-fault deformation, ranging from highly localized to completely distributed [e.g., Akyuz *et al.*, 2002; Hartleb *et al.*, 2002; Rockwell *et al.*, 2002; Treiman *et al.*, 2002; Duman *et al.*, 2003; Liu *et al.*, 2003; Haeussler *et al.*, 2004a, 2004b; Klinger *et al.*, 2005; Xu *et al.*, 2006; Van Dissen *et al.*, 2011; Oskin *et al.*, 2012] (O. J. Teran *et al.*, Geologic and structural controls on rupture zone fabric: A field-based study of the 2010  $M_w$  7.2 El Mayor-Cucapah earthquake surface rupture, submitted to *Geosphere*, 2014). These observations raise basic questions as to what controls the localization of fault slip near the surface. Dolan and Haravitch [2014] suggested that the structural maturity of the fault is the primary control, with slip on faults with large cumulative displacements remaining generally more localized at the fault trace than along ruptures on less mature faults. Significant variations, however, in the percentage of off-fault deformation within a single rupture on a fault or faults with the same structural maturity suggest that other factors also act to control the degree of slip localization at the surface.

In this paper we use high-resolution satellite imagery to analyze surface deformation patterns in the 2013  $M_w$  7.7 Balochistan, Pakistan earthquake. Specifically, we compare measurements of coseismic displacement from COSI-Corr subpixel optical image correlation, which documents the total surface deformation in ruptures over distance scales of hundreds of meters to tens of kilometers from the fault trace, to measurements of on-fault slip measured in high-resolution satellite images to determine the overall percentage of on-fault versus off-fault slip along the length of the rupture. For the purposes of this study, we use the term “off-fault deformation” (OFD) to describe all deformation—including secondary faulting and truly distributed deformation such as warping, distributed granular flow, and rotation—that occurs outside of the high-strain main strand of the surface rupture. We then compare these values to the type and relative age of near-surface materials (young

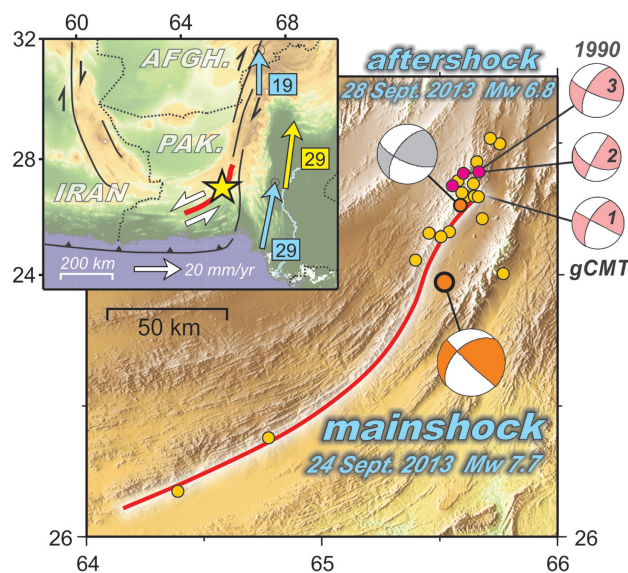


**Figure 1.** Topographic map showing the location of the 24 September 2013  $M_w$  7.7 Awaran main shock surface rupture (red line). USGS locations and focal mechanisms for the main shock (orange) and 28 September aftershock (gray) are shown, along with global CMT solutions for three earlier strike-slip earthquakes (red) which occurred at the NE-termination of the 2013 rupture in 1990 ( $M_w$  5.5–5.9). Small orange circles show USGS aftershock locations for the period following the 2013 rupture. Inset map shows the location of the Awaran rupture within the wider Arabia–India–Eurasia collision zone. Yellow star shows the location of the Awaran main shock. Yellow arrow shows the NUVEL-1 plate velocity of eastern Pakistan (Indian plate), relative to Eurasia. Blue arrows show GPS velocities from eastern Pakistan, relative to Eurasia [Mohadjer et al., 2010].

between N-S convergence in the Makran convergence zone to the west and N-S left-lateral strike slip on the Chaman transform system to the north and east [Lawrence et al., 1981] (Figure 1). The Makran convergence zone accommodates  $\sim 3$  cm/yr of convergence between Arabia and Eurasia [Reilinger et al., 2006], whereas the Chaman transform system accommodates  $\sim 3$  cm/yr of left-lateral strike-slip motion between India and Eurasia [Lawrence et al., 1981; Ambraseys and Bilham, 2003; Mohadjer et al., 2010; Ader et al., 2012; Szeliga et al., 2012].

The close association of the Hoshab fault with other reverse faults in the Makran region and its position at the boundary between a bedrock range front to the northwest and a sedimentary basin to the southeast suggest that either: (a) the Hoshab fault initiated as a thrust fault and later developed into a strike-slip fault; or (b) the fault alternates in its kinematics [Avouac et al., 2014]. Kinematic indicators observed in field studies of faults in the western Makran ranges show a bimodal distribution associated with early stage thrusting, and highly variable slip vectors associated with reverse faulting contemporaneous with sinistral strike-slip faulting [Platt et al., 1988], lending support to this latter possibility. Inversion of teleseismic waveforms shows that the Hoshab fault is subvertical in the northeast, but exhibits a gentler ( $\sim 50^\circ$ ) northward dip along its southwestern section [Avouac et al., 2014; Jolivet et al., 2014]. Despite this along-strike variation in fault dip, the 2013 rupture involved almost pure left-lateral strike slip, with only minor oblique reverse motion [Avouac et al., 2014; Jolivet et al., 2014]. Inverse fault slip modeling of the Landsat-8-derived displacement field indicates that the majority of slip occurred at relatively shallow depths ( $< \sim 10$  km), with the largest slip values occurring near the surface [Avouac et al., 2014; Jolivet et al., 2014]. This is in marked contrast to many other recent strike-slip ruptures that exhibit an apparent deficit in slip near the surface [e.g., Fialko et al., 2005; Sudhaus and Jonsson, 2011; Elliott et al., 2012], although the more strike-slip-dominated northern section of the 2008  $M_w$  7.9 Wenchuan rupture also exhibited higher slip nearer the surface [Tong et al., 2010].

### 3. Methods

We use two independent methods to analyze and measure patterns of surface deformation and displacements, as well as the structural style of the surface rupture and surrounding damage zone: (1) optical image correlation, using recently acquired Landsat-8 satellite images, and (2) visual inspection of high-resolution WorldView satellite images.

alluvium, older alluvium, and bedrock), and the distance from the fault to the nearest bedrock outcrop. Finally, we discuss these results in light of their implications for the behavior of near-surface materials during coseismic ruptures, geomorphic analyses of long-term slip patterns, probabilistic seismic hazards assessment (PSHA), and potential future microzonation of fault traces in developed areas.

## 2. Background

The 2013  $M_w$  7.7 Balochistan earthquake ruptured  $\sim 230$  km of the Hoshab fault in south-eastern Balochistan, Pakistan [U.S. Department of the Interior, U.S. Geological Survey, 2013; Avouac et al., 2014; Jolivet et al., 2014]. The Hoshab fault is located in the Makran accretionary complex and is part of a mechanical transition zone

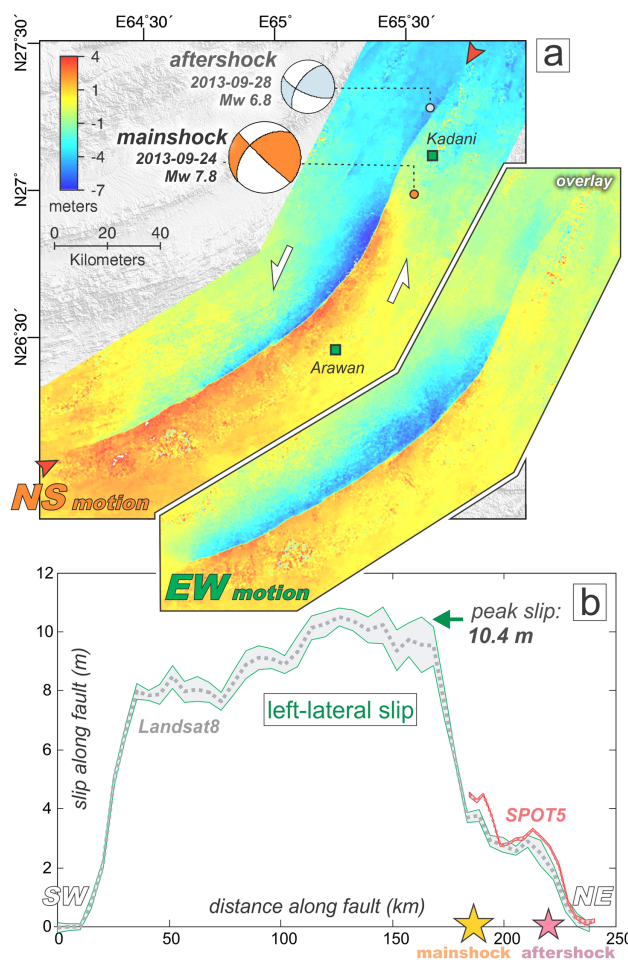


**Figure 2.** (a) EW and NS displacement maps covering the 2013 main shock surface rupture, calculated from the correlation of pre-earthquake and post-earthquake Landsat-8 satellite images using COSI-Corr. Displacements are given in meters. USGS focal mechanisms for the main shock (orange) and 29 September aftershock (gray) are shown. Red arrows show the end points of the along-strike-slip profile shown in Figure 2b. Left-lateral slip displacements calculated from the Landsat-8 correlation data are shown in green and gray. Red line shows slip measurements made from correlation of SPOT5 satellite images, which span the 28 September aftershock. Orange star shows the along-strike location of the main shock and the red star shows the 28 September aftershock.

ating several processing steps. Subpixel correlation of the two images using COSI-Corr takes advantage of an iterative, unbiased processor that estimates the phase plane in the Fourier domain [Leprince *et al.*, 2007a, 2007b, 2008; Ayoub *et al.*, 2009a]. This process produces two correlation images, each representing one of the horizontal ground displacement components in the East-West and North-South direction. In practice, this technique is able to resolve displacements as small as one tenth of the input pixel size (15 m for Landsat-8). Due to the excellent optical qualities of the Landsat-8 platform, however, and the minimal topographic residuals present in the correlations (a result of the nadir-looking Landsat-8 sensor), we were able to resolve displacements as small as 1/15 of a pixel (i.e., ~1 m). Stacking of fault-perpendicular displacement profiles can further increase the signal-to-noise ratio, thus allowing very well-resolved estimates of displacement along-strike (Figure 2b).

Due to the large displacements that occurred in this earthquake, coupled with local areas of higher noise resulting from topography or low image contrast, we used a multiscale window in our correlations, varying between 128 pixels and 32 pixels in dimension. Patches with the largest window size were correlated first, and if the correlation succeeded, smaller patches (decreasing by power of two) were correlated, while accounting for the previously found displacement. The process was iterated until the minimum window size was reached, or until the correlation failed, in which case the measurement found from the previous

### 3.1. Optical Image Correlation

Optical image correlation is used to determine the horizontal deformation produced by the earthquake at the surface. This technique compares two Landsat-8 satellite images of the region affected by the earthquake and measures any pixel shifts between them with subpixel precision. The short time period between the two image acquisitions (16 days; pre-earthquake: 10 September 2013, post-earthquake: 26 September 2013), coupled with minimal agriculture and vegetation in this desert environment, resulted in an excellent correlation between the two images (Figure 2a). The pre- and post-earthquake images were obtained from the USGS EarthExplorer website (<http://earthexplorer.usgs.gov/>), and correlated using the COSI-Corr software package (COSI-Corr, available for free download from [www.tectonics.caltech.edu/slip\\_history/spot\\_coseis/index.html](http://www.tectonics.caltech.edu/slip_history/spot_coseis/index.html)). Usually, COSI-Corr requires the user to orthorectify and coregister the two images before correlation. The USGS, however, distributes Landsat-8 images as an orthorectified product, thereby obvi-

larger size was kept and the process moved on to the next area (see the COSI-Corr user manual, available with download of the COSI-Corr software). Displacement measurements were made horizontally and vertically every 16 pixels, resulting in correlation map of 240 m resolution.

Additional noise was removed from the resulting EW and NS displacement maps by stripping out unlikely values (i.e., displacement of  $< -8$  m and  $> +8$  m, and values with a low signal-to-noise ratio). Due to a slight overlap of the charge coupled device (CCD) arrays on the Landsat-8 sensor, the correlations contain a striping artifact, which was removed by stacking and subtracting the average artifact signal from the correlations; this was done using the destriping tool in COSI-Corr with a manual rotation of  $-11.75^\circ$ . Finally, we used a  $3 \times 3$  median filter to further reduce noise, while preserving edges. Visual comparison of the filtered and raw displacement maps indicates our post processing steps do not artificially reduce our fault offset interpretation.

### 3.2. Mapping the Surface Rupture Trace and Width of Deformation Using High-Resolution Satellite Imagery

We used the panchromatic band of WorldView-1 and WorldView-2 high-resolution satellite images (with a nominal pixel resolution of  $< 0.5$  m [DigitalGlobe, 2014]) to visually map the surface trace of the 2013 rupture and measure the offset of geomorphic features. To account for any effects due to viewing geometry, we georeferenced and orthorectified the WorldView images using post-earthquake Landsat-8 images and an ASTER (Advanced Spaceborne Thermal Emission and Reflection Radiometer) GDEM (digital elevation model) with 30 m resolution (ASTER GDEM is a product of METI and NASA and was acquired through the USGS EarthExplorer website). After orthorectification, the pixel sizes for the WorldView images were between 0.505 and 0.594 m, providing a detailed view of the rupture trace. In all, we used 21 WorldView images for our visual analysis of the rupture. Of those, 17 were taken within 16 days of the earthquake, and all of the images were captured within 4 months of the event, so the effects of erosion of the fault scarp and any associated features are minimal. More information on all satellite images used in this study is available in the supporting information as file "ts01."

We mapped the major features of the rupture trace where it is visible in the WorldView images. To represent the width and style of surface deformation, we also mapped out zones of distributed deformation, including secondary fault strands, cracks, rotations, and obvious warping of the ground surface (Figure 4). Identification of such features is subject to the roughness of the terrain, image resolution, and the angle of the sun in each image. As such, the full extent of continuous deformation may not be represented in our mapping. Offsets of about 1 m or greater on a discrete planes were resolvable with the 0.5–0.6 m pixel sizes of the WorldView images.

We also noted whether or not each offset is on the "main" fault strand of the rupture trace. We define the main fault strand as the strand that accommodates more deformation and is more continuous along strike than surrounding strands. Where subparallel strands are approximately equal in both of these characteristics, neither was considered the main strand. We note that in some locations where no main strand can be established, we consider all deformation to be distributed, off-fault deformation, and we therefore assign a value of 0 m for our discrete main strand fault offset at those sites.

### 3.3. Measuring Offsets

We identified geomorphic features (e.g., channel thalwegs and edges, small ridges, gullies, and rills) along the surface trace of the 2013 rupture for which we could reliably measure offsets. We also measured several offset roads or footpaths, but such features are rare in this sparsely populated region. To measure each offset, we progressively back slipped one side relative to the other along the trace of the fault. In this way, we visually identified the maximum and minimum amounts of offset, identified as the points at which the restorations become sedimentologically implausible. These estimates are used as the error bounds shown in Figure 6. We also identified a preferred offset value for each feature, representing what we believe is the most likely amount of slip expressed on the fault strand at that location.

When measured, each offset was assigned a confidence rating of "A," "B," or "C" (Figure 3 and supporting information table ts03). A confidence of "A" indicates that the feature is sharply defined in the image and correlates unambiguously across the fault. A confidence level of "B" indicates that the geometry of the feature and the offset across the fault are less well constrained, and a confidence of "C" indicates that there is some ambiguity in reconstructing the feature across the fault, especially where the feature is warped or bent near the fault, and/or where the pre-offset geometry is difficult to determine. Figure 3 shows examples of offsets assigned each of these ratings.

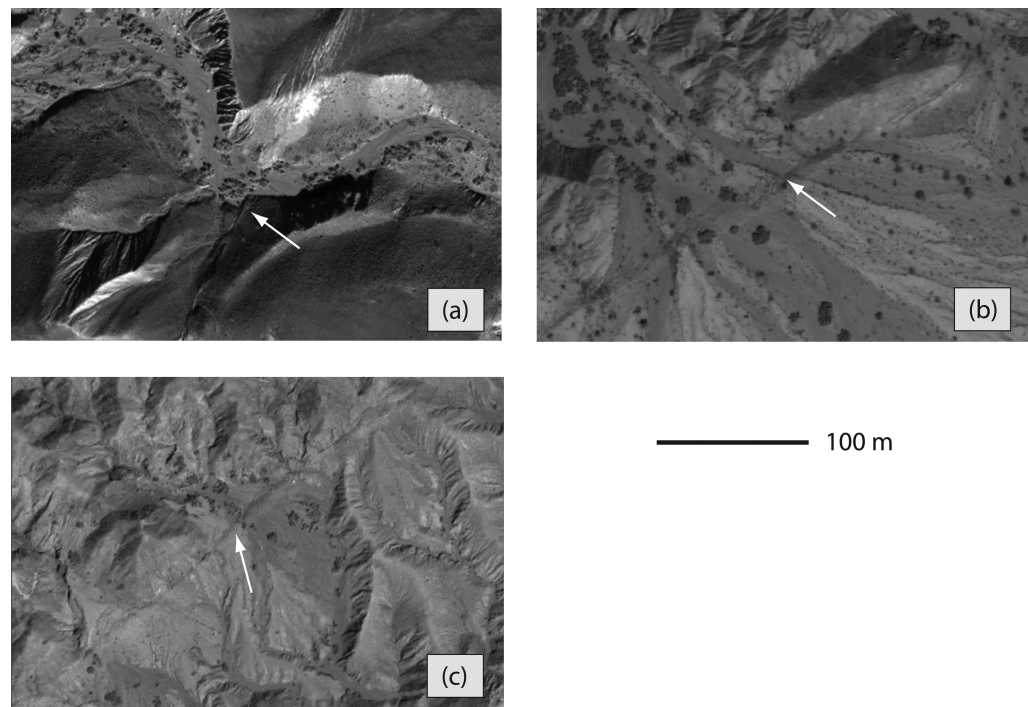


**Figure 3.** (a)–(c) WorldView images showing examples of geomorphic offsets with quality ratings “A,” “B,” and “C,” from best defined to least, respectively (see text for quality rating criteria). White arrows show the locations of the offsets that were measured. In Figure 3a, the river bank at the bottom of the slope can clearly be correlated across the fault and can be precisely restored by back slipping one side of the feature relative to the other. Although the fault trace is wider where it extends through the older alluvial fan to the north, the channel edge is offset cleanly, and the fault trace is relatively structurally simple at this location. In Figure 3b, although the fault trace is wider and more diffuse where it passes through the active alluvium and young fan sediments, the offset edge of the young fan can readily be correlated across the fault. In Figure 3c, the rupture trace is highly diffuse and it is relatively difficult to correlate the offset edges of the active channel edge where it is incised into young fan material to the SW across the fault (Imagery Copyright DigitalGlobe, Inc.)

Our analysis revealed a wide range of surface deformation patterns. In some locations, fault strands occur as discrete ( $<1$  m wide) fractures that are laterally continuous for up to 2 km. In contrast, at many locations, slip is not localized across a discrete fault plane, but rather is manifest as broader zones of diffuse deformation up to several tens of meters wide. Where there is a geomorphic feature that is highly linear for hundreds of meters on either side of the fault strand, we consider any clear bending over a relatively narrow fault-perpendicular aperture reproducing the scale at which geomorphic offsets are typically measured by field geologists ( $\leq \sim 5$  m) to be discrete and measurable fault slip. We measured the offset of such features by restoring them to their original geometry, as described above. Bending of geomorphic features over wider fault-perpendicular apertures (i.e.,  $>5$  m) could not be consistently recognized and measured. Therefore, any such measurements were not included in our analyses below. If a feature was deformed across a sufficiently wide fault-perpendicular aperture (typically  $> \sim 10$  m) such that two distinctly offset sides of the feature cannot be identified, the faulting is considered to be truly “distributed” and 0 m of fault offset was recorded in those instances. Thus, 0 m offset measurements do not necessarily preclude the presence of surface deformation. Rather, these “zero” measurements may represent locations where any surface deformation must be truly distributed and accommodated by secondary faulting and/or folding and other distributed deformation that cannot be readily identified at the scale of field measurements. For example, if a geomorphic feature (e.g., a small channel or bar) is deformed over a very wide zone such that the offset of the feature cannot be unequivocally distinguished from a geometry related solely to fluvial processes, the “offset” was recorded as 0 m.

To gain a better understanding of the pre-offset geometry of each of the geomorphic features crossing the fault, we referred to pre-earthquake color images available in Google Earth. These pre-earthquake images were not quantitatively differenced with the post-earthquake images, but instead were used to give a better sense of what the feature looked like before it was offset, reducing uncertainty in restoring the geomorphic features to their original geometry.

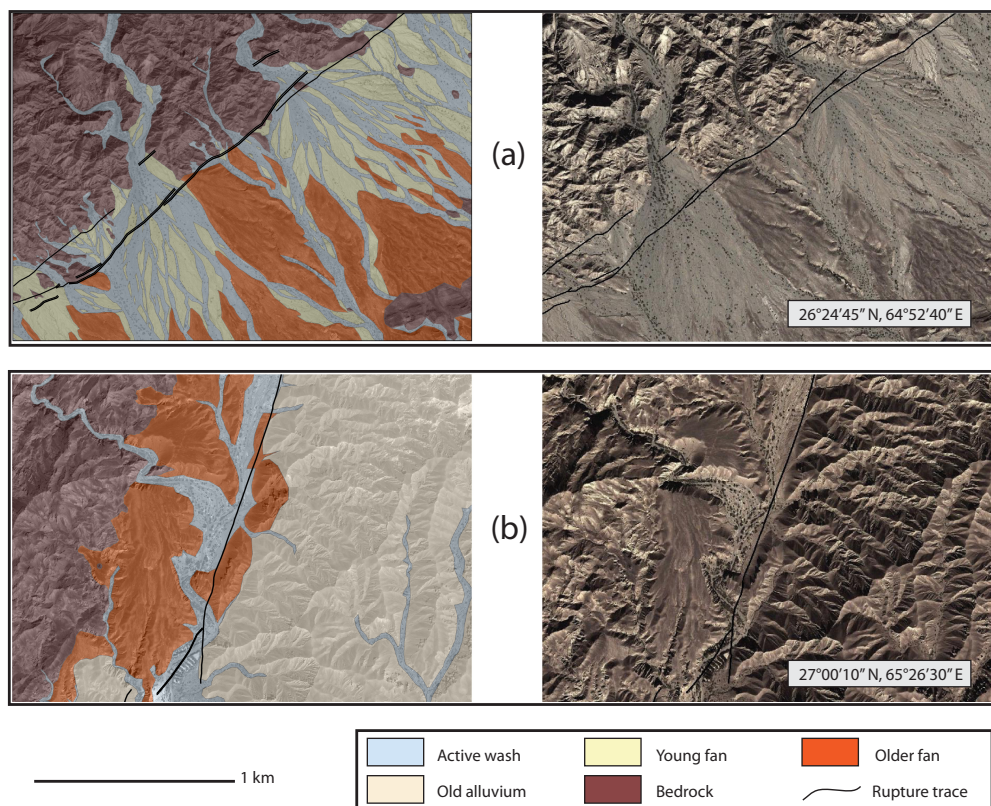


**Figure 4.** Examples of mapped surface material types. Figure 4a shows a section of fault where active wash sediments (blue), young alluvial fans (yellow), older alluvial fans (orange), and bedrock (burgundy) are present at the surface. The left image shows surface material types mapped on WorldView imagery; the right image shows a color image of the same area. Figure 4b shows active wash sediments, older alluvial fans, old consolidated alluvium (ivory), and bedrock mapped on WorldView imagery (left), as well as a color of that same area (right) [Google Earth, 2013, 2014] (Imagery copyright DigitalGlobe, Inc.).

In addition to measuring the offsets and assigning quality rankings, we made a qualitative assessment of the type and relative age of the surface material through which the rupture propagated at each measurement location. We classified the types of surface materials into five categories: Active wash sediments, young alluvial fans, older alluvial fans, old and probably well-consolidated alluvium, and bedrock. Active wash sediments are defined as loose sediments that are found near active or recently active rivers and that appear to have been deposited recently. Young alluvial fans exhibit surfaces that do not show significant desert varnish and are thus tan to light brown in color (appearing white to pale gray in the panchromatic images). Young fans have a distinct distributary drainage network and are uncut by any younger fan material. Older alluvial fans, in contrast, have significant desert varnish and are brown to dark brown in color (medium gray to black in panchromatic images). These older fans may have remnant distributary or post-fan tributary drainage networks and may be cut by younger alluvial fans. Old, compacted alluvium is brown (gray in panchromatic). It is distinct from “older fans” in that the overall geometries of the deposits are typically highly eroded and do have any obvious remnant fan morphology. Drainage patterns and topographic relief suggest that the old alluvium is more cohesive than old alluvial fans, though visual analysis provides no evidence of lithification (e.g., prominent, erosion-resistant bedding, and suggestions of cementation). Bedrock is identified by its relief, texture, color, and bedding characteristics, where present. Bedrock can range from white to dark brown in color. Examples of the different material types are shown in Figure 4.

## 4. Results

### 4.1. COSI-Corr Results

The EW and NS displacement fields from correlation of pre- and post-earthquake Landsat-8 images are shown in Figure 2a. Along-strike left-lateral displacement was measured from the EW/NS displacement field

by stacking fault-perpendicular profiles (Figure 2b). These data are provided in “ts02” in the supporting information. Stack width is 25 pixels, equivalent to 6 km on the ground. Error estimates represent the standard deviation (1-sigma) calculated from a trend that visually best fits the displacement on each side of the fault (calculated using the stacking tool in COSI-Corr). These error estimates do not take into account errors in the interpretation of the fault offset, which can be challenging in some areas. The location of highest slip occurs ~50 km SW of the main shock epicenter, with slip reaching up to  $10.5 \pm 0.3$  m (Figure 2b). The average slip determined from COSI-Corr measurements is  $6.7 +0.3/-0.4$  m.

A number of aftershocks occurred after the September 24 main shock, the largest of which was an  $M_w$  6.8 event that ruptured the same fault plane as the main shock on 28 September 2014 [Avouac *et al.*, 2014; Jolivet *et al.*, 2014]. To determine whether any additional surface deformation occurred during the 28 September aftershock, we also correlated two SPOT5 satellite images from 19 February 2004 and 29 September 2013, 1 day after the aftershock (image available in the supporting information as “fs01”). The displacement profile measured from this SPOT5 correlation indicates that no additional surface deformation occurred during the 28 September aftershock (Figure 2b). Therefore, slip in this aftershock likely occurred at depth. Consequently, we can be confident that our fault offset measurements determined from visual inspection of WorldView data do not include additional surface slip from the 28 September aftershock.

#### 4.2. Surface Rupture Displacements

From visual analysis of WorldView imagery, we measured 398 displacements along ~205 km of the rupture trace. Of the measurements collected, 279 were located on the main trace of the rupture, as defined above. A complete list of all measurements and their associated characteristics is provided in the supporting information as file “ts03.” Of these measurements, we observed a maximum displacement of  $11.4 +1.3/-2.1$  m. This is comparable to the  $10.5 \pm 0.3$  m maximum surface slip measured by our COSI-Corr measurement near that location, and similar to other COSI-Corr analyses of this earthquake [i.e., Avouac *et al.*, 2014; Jolivet *et al.*, 2014]. In places, slip along the rupture trace cannot be identified, or is less than the resolvable limit using these images (i.e.,  $\leq \sim 1$  m), as described above. At the northeastern end of the rupture (north of  $27^\circ 08' N$ ), the rupture trace is locally difficult to identify and measure. This is not surprising, as coseismic slip along this stretch was  $< 1-2$  m [Avouac *et al.*, 2014; Jolivet *et al.*, 2014, this study] and is therefore at or below the lower limits of resolution of the WorldView imagery. Our measurements of offset geomorphic features yield an average slip of  $4.2 +0.9/-1.0$  m.

#### 4.3. Structural Style and Width of Deformation Zone

Our field-scale satellite observations of the 2013 rupture trace reveal a great deal of complexity not captured in the COSI-Corr analysis. COSI-Corr correlations of Landsat-8 images show a relatively simple rupture trace with little structural complexity along a single fault [Avouac *et al.*, 2014; Jolivet *et al.*, 2014, this study]. Our visual analysis of WorldView imagery, however, reveals many steps, bends, and complexities at scales ranging from meters to kilometers.

Although the rupture trace is single-stranded at some locations (particularly between the southwestern end of the surface rupture and  $64^\circ 23' E$ , and near the middle of the rupture between  $26^\circ 40' N$ ,  $65^\circ 14' E$  and  $26^\circ 56' 30'' N$ ,  $65^\circ 25' E$ ), it is multistranded along much of its length. In some instances, the multistranded nature of the rupture is clearly due to broad-scale structural control, as in the case of an 8-km-wide restraining step at  $26^\circ 28' 00'' N$ ,  $64^\circ 58' 30'' E$ , and a 6-km-wide releasing bend at  $26^\circ 36' 30'' N$ ,  $65^\circ 10' 30'' E$ . For most of the rupture length, however, there is no clear association between the broad-scale structure of the locality and the style of faulting.

The total width of deformation along the fault that is resolvable in the WorldView images ranges from narrow and highly localized to very wide and highly distributed (Figure 5). Where deformation is extremely localized, all visible offset is localized on a single strand that is less than a meter wide. At its widest, however, visible deformation locally spans widths of up to nearly 800 m, measured perpendicular to the main fault trace. These broad zones of deformation typically have one or more fault strands within them, which occur as discrete or meters-wide zones of more highly concentrated shear. The transition from localized to highly distributed slip can occur in tens to hundreds of meters distance along strike. We note that where it is widely distributed, deformation is mostly observed in the hanging wall of the northwest-dipping fault.

The fault strands themselves exhibit a variety of characteristics. At their most localized, strands can occur as discrete planes of shear, less than a meter wide. Other strands occur as meters-wide zones of concentrated

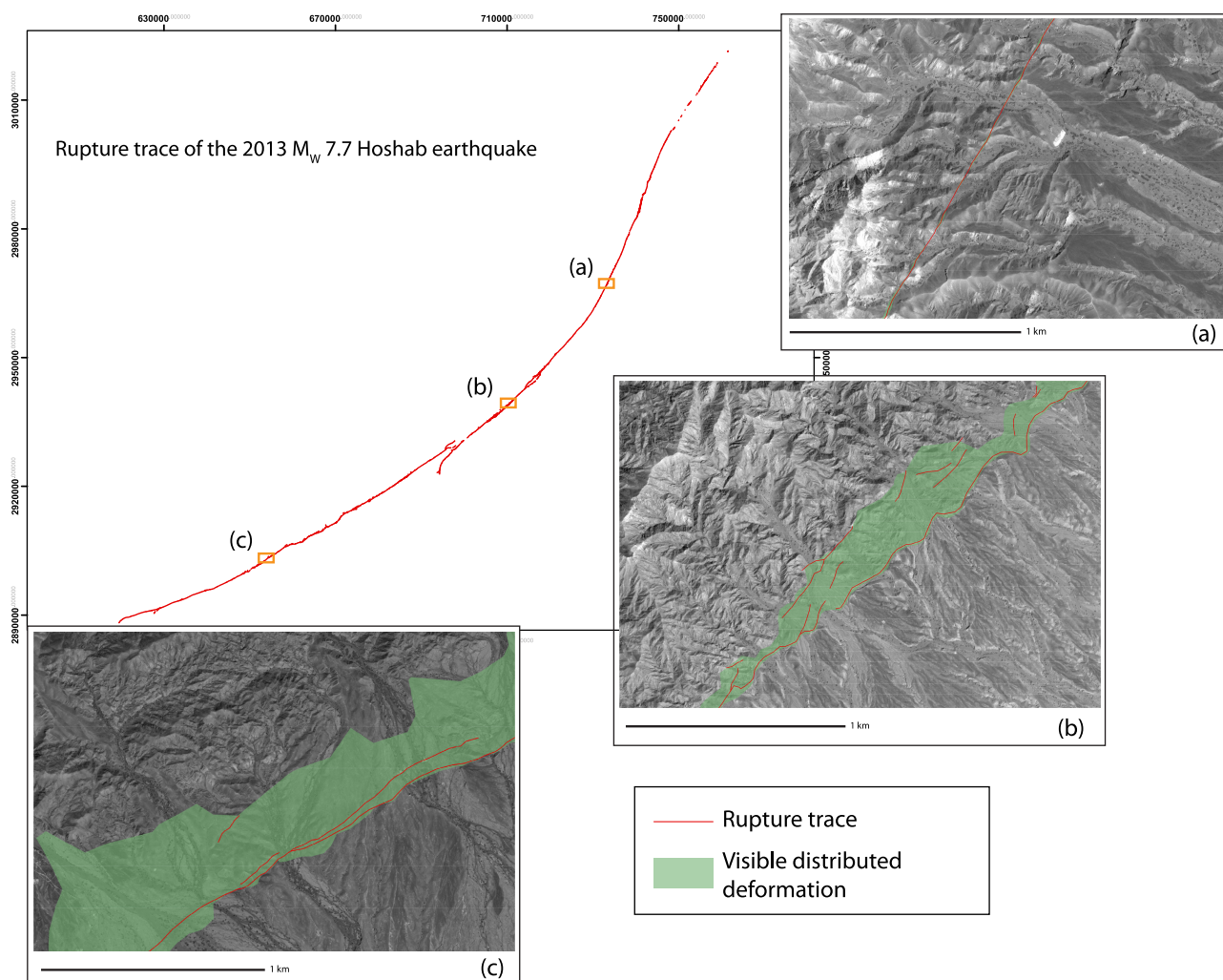


**Figure 5.** Fault traces and zones of continuous deformation visible in optical imagery. Zones of visible deformation range from (a) <1 m to (c) ~800 m in width. The structural style of the rupture traces range from (a) structurally simple to (b, c) structurally complex (Imagery Copyright DigitalGlobe, Inc.).

deformation within the broader fault zone. The wider types of fault strands are more common in unlithified, poorly consolidated sediments (i.e., active washes, young alluvial fans, and older alluvial fans). Riedel shears are locally observed in active wash sediments and across young alluvial fans. In some active river sediments, the fault trace is visible on either side of a river, but is not visible within the river bed itself, even where the rupture trace does not appear to have been washed away by the river. Presumably, deformation is so highly distributed in those sediments that it is not manifest as a distinguishable rupture trace.

## 5. Discussion

### 5.1. Off-Fault Deformation of the 2013 Rupture

Comparison of our field-scale measurements of offset geomorphic features, which record the component of slip localized along the main strand of the fault, to the total surface displacement across the entire width of the zone of surface deformation obtained from COSI-Corr analysis allows us to quantify the percentage of off-fault deformation associated with the rupture. We observe significant differences between the field-scale measurements taken along the main strand of the fault and the total slip measured using COSI-Corr (Figure 6). Although we would expect relatively minor discrepancies between the two data sets due to the smoothing effect of the correlation window used in COSI-Corr, there are several large stretches of the rupture where the main trace field-scale measurements are significantly lower than the

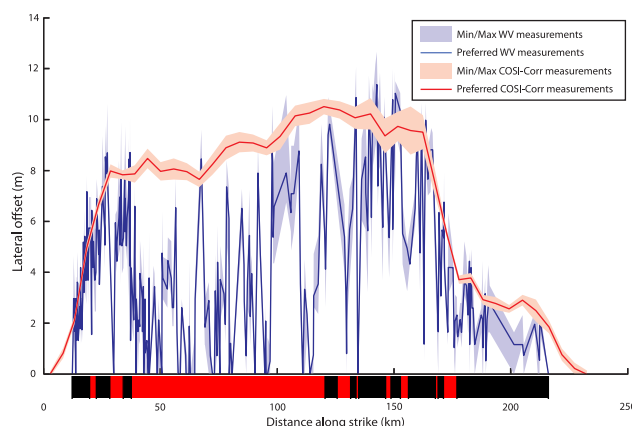


**Figure 6.** Comparison of offset measurements as a function of distance along the rupture. Red line represents offset measurements from COSI-Corr analysis of Landsat-8 data. Blue line shows offset of geomorphic features measured along the main trace of the rupture as determined by visual analysis of WorldView <0.6 m resolution satellite images. Shaded fields represent the maximum and minimum reasonable slip values. The colors along the bottom of the figure represent structurally simple (black) and structurally complex (red) sections of the fault.

increases, the ratio of slip along the fault trace relative to geodetically inferred slip at depth (referred to as the “surface slip ratio,” or SSR) also increases. The SSR is thought to be a function of the structural maturity of the fault, that is, as a fault accumulates more slip, the number of discontinuities decreases and the fault structurally matures, gradually becoming smoother [Wesnousky, 1988; Stirling *et al.*, 1996].

To the best of our knowledge, there are no estimates of cumulative displacement on the Hoshab fault. Many southward-draining, deeply incised rivers cut north-to-south across the Hoshab range, thereby suggesting these rivers are antecedent, that is, predating uplift of the range. We suggest that in addition to any early thrust displacements, the Hoshab fault has accommodated at least 5.6 km, and likely ~11 km, of left-lateral strike-slip displacement. This is shown particularly well by the offset of a major river valley at 27°19'15"N, 65°39'31"E (Figure 7). This major drainage is offset by ~5.6 km along the Hoshab fault, extending toward the fault at near right angles along both the southeastern (downstream) and northeastern (upstream) reaches. This geometry suggests that the leftward deflection of the river at the fault records true fault offset. This offset is a minimum, however, as it does not include any distributed component of near-surface deformation. Indeed, consistent 4-km-wide, convex-to-the-west bends in all of the numerous drainages that cut the Hoshab Range in this area suggest that significant additional strike slip (manifest as strike-slip “drag folding”) is distributed to the northwest of the Hoshab fault. For example, the upstream reach of the major drainages offset by 5.6 km exhibits a very linear NE-trending reach upstream of the large bend in the river. Projecting this trend to the Hoshab fault indicates that the apparent folding of the river NW of the Hoshab fault has accommodated an additional 4.8 km of distributed left-lateral strike slip, for a total of ~10.4 km of cumulative strike slip on the Hoshab fault at this location. A similar ~11 km offset of bedrock 40 km to the NE along the Hoshab fault suggests that this value may record cumulative strike slip over much of the section of the Hoshab fault that ruptured in the 2013 earthquake (Figure 7).

These measurements indicate that the Hoshab fault is a structurally immature fault in terms of its cumulative strike slip. Other nearby faults in this system also exhibit small amounts of cumulative strike slip. For example, left-lateral offset of a distinctive bedrock unit on a related fault to the southwest of the river valley that is offset 5.6 km suggests cumulative left-lateral displacement of ~6 km on that strand (Figure 7). Similarly, offset of a bedrock ridge on another strand to the east of the Hoshab fault indicates a total of ~4 km of displacement. Thus, despite being geomorphically well expressed in the landscape, the Hoshab fault appears to be a structurally immature fault in terms of its total strike slip.

Based on the findings of Dolan and Haravitch [2014], we would expect 40–60% of the total slip at depth for the earthquake to be localized at the surface for a fault with 6–11 km of cumulative strike slip. Following the method of Dolan and Haravitch [2014], we define the surface slip ratio as the ratio of integrated slip (the area

corresponding COSI-Corr measurements (most notably the region from 35 to 90 km along strike, measured from the southwest end of the rupture; Figure 6). We attribute this “missing fault slip” to deformation that is not localized on the main trace of the fault, but rather is distributed throughout the zone of surface deformation.

Recent studies suggest that the ratio of slip at the surface to slip at depth is primarily determined by the structural maturity of the fault. Dolan and Haravitch [2014], for example, compared the ratio of surface slip to slip at depth as a function of cumulative fault displacement for six large ( $M_w$  7.1–7.9) strike-slip earthquakes. They found that as the cumulative strike slip (i.e., structural maturity) along a fault

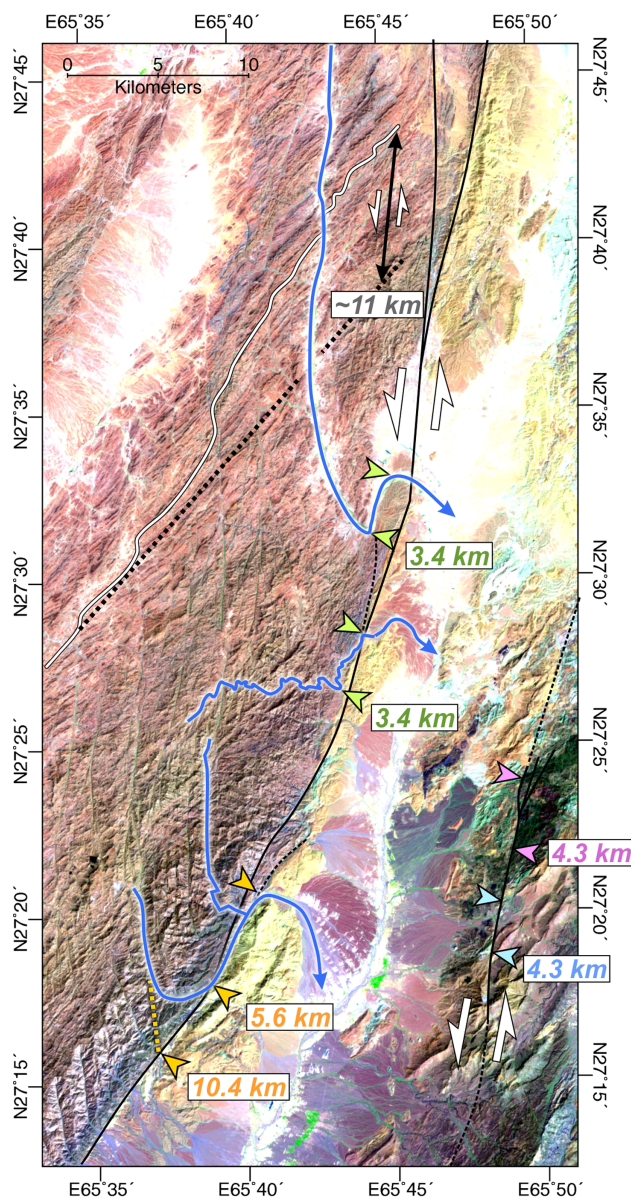


**Figure 7.** Landsat-8 satellite image (bands 751), showing the geology of the NE-end of the 2013 main shock rupture. Black lines show active faults, and blue lines highlight certain rivers which have been offset by the Hoshab fault. Multicolored pointers highlight offset drainage and geology at different locations. See text for discussion.

may have served to smooth the rupture plane and may have enhanced the overall structural maturity of the fault beyond the ~11 km of strike slip we document.

To more closely examine the influence of structural complexity on the percentages of off-fault deformation along the rupture, we divided the surface rupture into 10 segments based on whether the surface trace along those sections of the fault was structurally complex or structurally simple (Figure 6). In this context, when we describe the surface expression of faulting, we are not referring exclusively to large zones of structural complexity, such as fault step overs, bends, or intersections. Rather, we are referring to stretches along the fault that exhibit multiple strands, rotations, and warping (see Figure 5 for examples). For each structurally simple and structurally complex stretch of fault, we divided the area under the curve of the WorldView measurements by that of the COSI-Corr measurements over that stretch of fault, in a manner analogous to the way that we calculated the SSR. Our analysis demonstrates that, as might be expected, there is a clear difference in

under the curve of surface slip measurements as a function of distance along the rupture trace) measured from offset geomorphic features (blue lines in Figure 6) to that the total surface displacement, including any off-fault, distributed deformation measured by COSI-Corr (red lines in Figure 6) over the same 205 km long stretch of the rupture for which the data sets overlap. This definition yields an SSR value of  $0.56 \pm 0.16 / -0.15$  (Table 1), which is near the upper range expected for a fault with only 6–11 km of cumulative strike slip [Dolan and Haravitch, 2014].

Our estimate of cumulative strike slip on the Hoshab fault does not, however, include any reverse slip that has occurred along this fault. This additional slip may serve to enhance, somewhat, the overall level of structural maturity of the fault. We have no constraints on the amount of reverse slip on the Hoshab fault, nor the precise timing for the onset of strike slip, so it is difficult to predict what effect the extent to which reverse slip would smooth the rupture plane. It is also difficult to predict the effects of structural features such as large striations, mullions, and structural segmentation oriented in a geometry that would allow dip-slip motion but would resist oblique motion. Inversions for slip distributions by Jolivet *et al.* [2014], however, show that once nucleated, the propagating 2013 rupture did not encounter any geometrical obstacles, nor was it hindered by any significant segmentation. Thus, it appears that cumulative reverse slip experienced by the Hoshab fault did not generate significant strike-perpendicular barriers to smooth rupture propagation, but rather

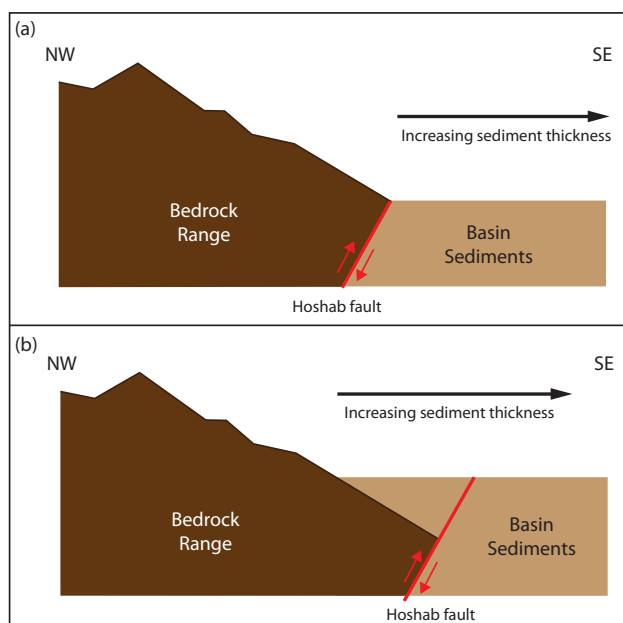


**Figure 8.** Schematic cross section showing increasing sediment thickness basin ward of the range front. Range of different configurations is shown by (a) where the fault traces comes to the surface at the range front and (b) where the fault trace is located out in the alluvium to the southeast of the surface rupture. We see examples of both along the surface rupture. In both instances, sediment thickness increases basin ward as distance from bedrock increases, due to the reverse component of slip that characterizes at least some of the earlier activity along the Hoshab fault (see text for discussion). The slope of the bedrock/sediment contact shown in the diagram reflects the average slope of the range front. Fault dip shown reflects the average dip of the Hoshab fault ( $\sim 60^\circ$ ) inferred from inversion of teleseismic waveforms [Jolivet *et al.*, 2014]. The general linearity of the surface rupture trace as it crosses topography suggests that the fault maintains a relatively steep dip all the way to the surface, as shown in the diagram.

ratio akin to the local surface slip ratio (LSSR) described by Dolan and Haravitch [2014]. For structurally simple sections of the fault, we calculate an LSSR of 0.8, indicating that, on average,  $\sim 20\%$  of total surface deformation is accommodated by distributed processes off the main strand of the fault. In contrast, for structurally complex sections of the fault, we calculate an LSSR of 0.4, indicating that more than half of the total surface displacement is accommodated off the fault. These ratios (Table 1) demonstrate the control exerted by the local structural complexity of the fault on the localization of strain along a fault rupture, with greater strain localization in areas of greater local structural complexity. Such along-strike differences in structural expression will, if repeated over numerous earthquake cycles, become manifest in the landscape. Careful geomorphic mapping of other faults should thus be able to distinguish between fault sections where surface slip will be relatively more distributed or more discrete.

### 5.2. Surface Material Control on Strain Localization

Although the structural immaturity of the Hoshab fault exerts a primary control on the localization of deformation, variations in the percentage of off-fault deformation along the rupture suggest that there are other controls at work [Dolan and Haravitch, 2014]. Recent experimental studies [e.g., Ma, 2008; Ma and Andrews, 2010; Kaneko and Fialko, 2011] show that the type of material through which a rupture propagates strongly affects the amount of distributed deformation. Specifically, slip is expected to be more localized where a rupture passes through bedrock than where it passes through poorly consolidated or unconsolidated sediments, due to the velocity strengthening nature of these materials. This phenomenon has been observed in several recent large-magnitude surface ruptures. For example, in the 2010  $M_w$  7.0 Darfield, New Zealand, earthquake, the average surface displacement was  $\sim 2.5$  m, with maximum offsets reaching 5 m, yet there was little or no discrete faulting [Van Dissen *et al.*, 2011; Duffy *et al.*, 2013]. Instead, deformation was distributed over 30–300 m wide zones, probably due to the thick sequence of poorly consolidated alluvial gravels

the percentage of on-fault slip between the structurally simple and structurally complex parts of the surface rupture. Specifically, the average ratio of slip localized on the main rupture trace to the total deformation is 0.74 for structurally simple segments of the rupture, and 0.44 for structurally complex segments (Table 1). We emphasize that these ratios are averages over 3–82 km stretches of the fault, and within any one of those zones the ratio can range anywhere from 0–100% on-fault, localized deformation. Nevertheless, on average, even along stretches of fault where the trace is relatively structurally simple, approximately one-quarter of the total fault slip that reached the surface was expressed as distributed deformation surrounding the fault.

To examine this relationship more precisely, we compared each of our 279 field-scale measurements along the main trace of the fault to the amount of surface slip estimated by COSI-Corr analysis at each measurement location. The average of these ratios for measurement at structurally simple locations along the rupture and at structurally complex locations yields a

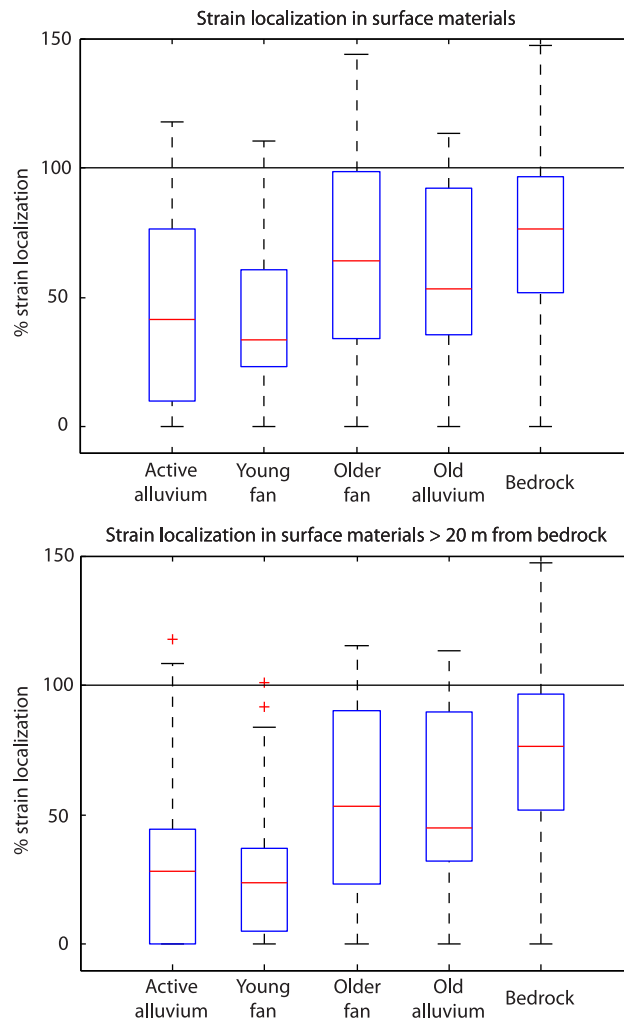


**Figure 9.** Box and whisker plots represent the percent of total strain localized on the main trace of the fault at individual measurement locations grouped by the type of surface material in which they are located. Locations within obvious structural steps and discontinuities have been excluded. Red lines represent the median of localization estimates in each group; blue boxes represent the 25th and 75th percentiles, whiskers represent the 1st and 99th percentiles, and red crosses represent outliers at the 99th percentile. When considering strain localization in all such measurements, there is a general tendency for strain to be more localized in younger sediments, but in (a) the trend is weak. If we use distance to the nearest bedrock outcrop as a proxy from sediment thickness, however, we see that localization generally increases with increasing age of the surface material in materials >20 m (b) from the nearest bedrock outcrop (bedrock samples are shown for comparison). We attribute this observation to increasing sediment incipient lithification with age, resulting in sediment deposits that are stronger and therefore better able to localize coseismic deformation. This effect is manifest in thicker sediments because they are less subject to the strain localization patterns in the underlying bedrock.

through which the rupture propagated [Van Dissen et al., 2011]. Similarly, recent studies show dramatic variations in the style of deformation and magnitude of discrete slip associated with the 2010  $M_w$  7.2 Sierra El Mayor-Cucapah earthquake due to variations in the type of near-surface material (Teran et al., submitted manuscript, 2014). In particular, remote sensing techniques revealed  $\sim 2$  m of coseismic slip occurred along the southern part of the 2010 El Mayor-Cucapah rupture [Wei et al., 2011; Oskin et al., 2012], yet no discrete faulting was observed at the surface where the rupture passed through the thick sediments of the Colorado River delta [Oskin et al., 2012] (Teran et al., submitted manuscript). Conversely, bedrock has been shown to localize deformation. For example, the highest coseismic slip values associated with the 1999  $M_w$  7.1 Hector Mine earthquake were observed where strain was most localized where the rupture passed through the bedrock all the way to the surface through the Bullion Mountains [Treiman et al., 2002; Milliner et al., 2014; C. W. Milliner et al., manuscript in preparation, 2014]. Thus, it appears likely that the type (more specifically the strength) of the near-surface material through which the 2013 rupture on the Hoshab passed has an effect on strain localization.

To test whether or not the type of surface material exerts a control on the localization of deformation for this rupture, we examined the amount of slip localized on the main trace of the fault as a function of the type of near-surface material from which each offset was measured. As described above, the surface material types were classified as active wash sediments, young alluvial fans, older alluvial fans, old compacted alluvium, and bedrock. Intuitively, one would expect older sediments to be mechanically stronger than younger sediments because they have had more time to become more indurated, and bedrock is expected to be stronger than unlithified sediments. While we make no attempt at quantifying the exact mechanical properties of these materials, we use their relative ages as a proxy for their relative strength. We would

**Table 1.** Mean Fault Slip and Surface Slip Ratios

	Minimum	Preferred	Maximum
Mean slip using geologic measurements (m)	3.23	4.18	5.22
Mean slip using COSI-Corr measurements (m)	6.33	6.69	7.04
Surface slip ratio (SSR), after Dolan and Haravitch [2014]	0.41	0.56	0.73
Surface slip to total slip along structurally simple fault segments		0.74	
Surface slip to total slip along structurally complex fault segments		0.44	
Local surface slip ratio (LSSR) for structurally simple fault segments		0.81	
Local surface slip ratio (LSSR) for structurally complex fault segments		0.40	

expect strain to be significantly more localized in older materials and bedrock. If this hypothesis is correct, off-fault deformation would increase from bedrock to old alluvium to older fans and surface deformation would be the most distributed in the youngest, least-consolidated sediments. In this analysis, we do not con-

sider the grain sizes, sorting, or mineralogy of either the sediments or the bedrock, as those characteristics cannot be inferred from satellite imagery.

We estimated the percent localization of strain (100% - percentage OFD) for each of the field-scale measurement locations along the main strand of the fault. To compare each field-scale measurement to the total expected slip at that location, we interpolated between the nearest two COSI-Corr measurements using a simple linear interpolation. We then differenced the preferred value for each field-scale measurement with its corresponding COSI-Corr slip value and normalized that difference to the expected slip. To avoid locations that are obviously structurally controlled (e.g., the restraining step at 26°28'00"N, 64°58'30"E and the releasing bend at 26°36'30"N, 65°10'30"E), we omitted points in and near large fault steps and structural discontinuities.

When we compared all relevant estimates of strain localization grouped according to their type of surface material, we observed a general tendency for strain to be more localized in younger sediments, but the trend is weak (Figure 9a). We hypothesize, however, that the thickness of the material also plays a significant role in localizing or delocalizing deformation. For example, a very thin layer of sediment overlying bedrock might not have sufficient thickness to distribute deformation, and the localization of strain in that sediment layer would simply reflect the localization of strain in the underlying bedrock. A thicker package of sediment, in this instance, would more effectively distribute deformation. From the WorldView images, we have no direct indication of sediment thickness at any given location. Instead, we use the distance from the offset measurement location to the nearest bedrock outcrop as a proxy for sediment thickness. We suggest that use of this distance-to-nearest-bedrock proxy is warranted as the Hoshab fault exhibits a clear history of reverse slip, uplifting bedrock to the northwest, while sediments were deposited basinward to the southeast. This simple relationship is schematically illustrated in Figure 8. Moreover, we do not attempt to quantify the precise relationship between sediment thickness and distance to bedrock, but would nevertheless expect the sediments to be generally thicker farther from the edges of the river or basin. When we compare localization in different sediment types for measurements more than 20 m away from the nearest bedrock outcrop, we see that strain is indeed more localized in older sediments than in younger sediments (Figure 9b), implying a positive correlation between a material's age and its ability to localize deformation. As expected, strain is generally more localized in bedrock than in any of the different sediment types.

The tendency for younger and thicker sediments to distribute deformation does not, however, apply without exception (Figure 9). At some locations, strain is extremely localized in active wash sediments at relatively large distances from the nearest bedrock outcrop. At those locations, the depth to bedrock may be shallower than indicated by distance to the nearest bedrock outcrop. Alternatively, the more localized parts of the surface rupture may simply reflect sections of the underlying fault that are structurally simpler than other sections. For instance, we observe locations in bedrock where strain is highly distributed, reflecting localized structural complexity of the fault. Nevertheless, although the relative local abundance of such complexities in the bedrock underlying different types of sediments may play some role in determining strain localization, the consistency of the percentages of strain localization in different sediment types along

the entire length of the fault strongly suggests that the sediment type and relative thickness of the sediment act as a basic control on the distribution of near-surface deformation.

A potential source of bias in this analysis arises from the method of sampling. Measurements were taken wherever a geomorphic piercing point is available. If there are many piercing points in a sediment package where localization happens to be controlled by other factors (e.g., structural discontinuities) then the feature could be oversampled and any statistics will be biased toward that feature. We assume, however, that the 278 main-strand measurements (excluding those in zones of obvious structural control) taken over a 205 km length along the main trace of the surface rupture are sufficiently numerous and well-spaced that they accurately represent the localization of strain in each type of surface material.

Further study is required to examine the effects of cumulative slip in each type of surface material. In this analysis, we treated all types of surface materials across the rupture as though they have experienced the same amount of slip. Naturally, however, materials old enough to have experienced several earthquake cycles will have accumulated more deformation than freshly deposited materials. Pre-earthquake images show evidence of faulting from previous earthquakes in some of the older fans, in old alluvium, and in bedrock, whereas younger materials (i.e., active wash sediments and young alluvial fans) were mostly undeformed prior to the 2013 surface rupture. Such prior deformation in older materials would serve to further enhance strain localization, complementing the effects of strengthening due to compaction and induration.

Overall, our comparison of strain localization with surface material type strongly suggests that, given sufficiently thick sediments, there is a correlation between percent OFD and material type, as suggested by models [e.g., *Ma*, 2008; *Ma and Andrews*, 2010; *Kaneko and Fialko*, 2011] and field observations [e.g., *Treiman et al.*, 2002; *Shelef and Oskin*, 2010; *Van Dissen et al.*, 2011; *Oskin et al.*, 2012; *Duffy et al.*, 2013; *Dolan and Haravitch*, 2014]. The precise degree of influence that near-surface material properties and thickness have on strain localization provides fertile ground for future research, and many more observations such as those detailed above from other specific ruptures are needed.

### 5.3. Implications for the Use of Fault Slip Rate Studies Based on Geomorphic Offsets

In light of the observations described above, it is clear that measuring only the slip localized on the main strand of a fault will significantly underestimate the total slip associated with a rupture event. This has important implications for the proper understanding and use of slip rate studies based on offset geomorphic markers along structurally immature faults, as such measurements may significantly underestimate the total displacement at a site. Consequently, any slip rates based on these offset measurements will also be underestimated [e.g., *Dolan and Haravitch*, 2014]. This observation, in turn, will affect any comparisons between geologic fault slip rates and geodetic measurements in the search for transient strain accumulation.

Special care should be taken when interpreting slip rates based on offsets in thick, relatively young sediments, as sediments of sufficient thickness tend to distribute deformation. Intuitively, the effect of distributed, off-fault deformation is likely to be smaller for structurally mature faults than it is for structurally immature faults. But in general, we suggest that all slip rates that do not account for off-fault deformation should be considered minima.

When determining slip rates based on measurements of offset geomorphic features, however, we are hesitant to suggest a numerical correction factor based on any of the factors mentioned above (i.e., structural maturity, near-surface material type, and thickness), as further study is required to better understand the effects of each of them. With a better understanding of the percentage of off-fault deformation and its controls, future work should be able to more accurately constrain the degree to which geological slip rates based on surface offsets underestimate the true fault slip rate at seismogenic depths.

### 5.4. Implications for Seismic Hazard

Studies of distributed versus localized deformation have critically important implications for probabilistic seismic hazards assessment (PSHA). Because fault slip rates are often a primary input in PSHA models, it is important to understand how slip at depth along a fault is manifested as slip at the surface, and especially the degree to which it is localized on the main surface trace of a fault such as might be used by a geologist to measure an offset for a slip-rate study. As discussed above, some percentage of the total deformation associated with an earthquake will likely be distributed away from the main trace of the surface rupture. Consequently, slip rate studies based solely on main-strand offsets could lead to systematic

underestimation of the true fault slip rate, resulting in a commensurate underestimation of hazard. This is especially true when determining slip rates of small cumulative strike-slip displacement (<25 km) faults [Dolan and Haravitch, 2014]. As seen in the case of the 2013 rupture along the Hoshab fault, accounting solely for slip manifest along the main trace of the rupture could lead to an underestimation of the total surface slip associated with the main shock by approximately 45% of the true value. The 2013 rupture of the Hoshab fault also demonstrates that special care must be taken when measuring geomorphic offsets along ruptures that propagated through thick, unconsolidated sediments, as these deposits tend to distribute deformation. Any underestimations of true fault slip rates resulting from failure to account for distributed, off-fault deformation may lead to underestimation of the hazard posed by the fault, with obvious implications for the built environment, especially for faults near densely populated areas.

Additionally, surface slip-per-event data are commonly used to estimate paleo-magnitudes through comparisons with regressions of slip to  $M_w$ . In light of the evidence above, such paleo-magnitude estimates may substantially underestimate the true magnitude of earthquakes, especially on structurally immature faults and in studies based on point displacements taken from either very young and/or thick sedimentary sections. If that is the case, then the seismic risk to an area may be underestimated.

Finally, studies addressing the style and magnitude of off-fault deformation have important implications for the built environment, particularly in terms of the future development of microzonation maps for earthquake-resistant building design. Specifically, it matters greatly if the expected displacement in a probabilistic design earthquake at a specific site will be highly localized along a single, main fault strand, or highly distributed over a wide zone. As discussed above, studies relating various parameters (e.g., fault structural maturity, detailed structural geometry of the fault, sediment type, and thickness) that may control such deformation patterns will provide the basic information necessary to properly evaluate expected patterns of surface deformation in future large earthquakes. Ultimately, data derived from analysis of these relationships for numerous earthquakes could lead to a statistically meaningful understanding of the likelihood that any of these parameters—all of which could potentially be documented in advance of future earthquakes—will generate more-discrete or more-localized surface slip at any particular study site. In turn, these results could be used to construct microzonation maps that would capture the expected style and distribution of surface deformation at a site, thus potentially reducing damage to infrastructure in future earthquakes.

## 6. Conclusions

Comparison of slip measurements made at different scales using high-resolution WorldView satellite imagery and COSI-Corr subpixel image correlation reveal significant complexity in surface deformation patterns during the 2013  $M_w$  7.7 Balochistan, Pakistan earthquake. Specifically, fault slip measurements of geomorphic features along the main trace of the 2013 Hoshab fault rupture and measurements of total surface deformation from COSI-Corr analysis show that  $56 \pm 16\%$  of the deformation is localized on the main strand of the rupture, indicating that almost half of the deformation was accommodated by distributed deformation in the damage zone surrounding the fault. Estimates of cumulative strike slip on the Hoshab fault suggest total sinistral motion of  $\sim 6\text{--}11$  km, indicating that this is a structurally immature fault. The  $\sim 56\%$  on-fault deformation is generally similar to the ratio of on-fault to off-fault slip expected for a fault with this degree of structural maturity [Dolan and Haravitch, 2014]. Thus, although the structural maturity of the Hoshab fault appears to be the dominant control on the degree of slip localization at the surface, large variations in along- and across-strike patterns and magnitudes of on-fault versus off-fault deformation indicate that other factors also acted to control the behavior of co-seismic displacement during the 2013 main shock. Our analysis of the relationship between surface deformation patterns and the relative age and thickness of different types of fluvial and alluvial sedimentary units relative to bedrock along the surface rupture indicates that these factors exert a strong secondary control on patterns of surface deformation, with more localized deformation in bedrock and older and thinner alluvial strata. Conversely, surface deformation in younger and/or thicker fluvial and alluvial deposits tends to be much more distributed.

These observations have basic implications for a range of disciplines, including the proper understanding and use of geologic slip rates, especially as when used as inputs to probabilistic seismic hazard assessments, and the mechanical behavior of near-surface materials during large coseismic ruptures, which in turn has significant implications for the built environment and potentially for radiation of strong ground motions.

Moreover, if the controls on patterns of surface slip localization and delocalization can be determined with sufficient confidence through additional studies similar to this one, these results will constitute important inputs into future studies of microzonation for the built environment, potentially demonstrating in advance where surface slip will be more localized, and where it will be more distributed.

### Acknowledgments

This research was funded by the U.S. National Science Foundation (NSF EAR-1147436 to Dolan). WorldView satellite imagery was obtained through the NSF-funded Polar Geospatial Center at the University of Minnesota, and we would like to thank Paul Morin, Thomas Juntunen, Spencer Niebuhr, and Cole Kelleher for their much appreciated assistance with obtaining these data. We thank the USGS EarthExplorer website, which greatly simplified access to the Landsat-8 data used in this study. SPOT5 images were obtained through the CNES-sponsored ISIS program using funds provided by an internal lab grant awarded to Hollingsworth. We thank Stephen Hosford at CNES for his help in acquiring SPOT5 images in the days following the earthquake. Magali Aufferve also provided assistance obtaining SPOT5 images. Finally, we thank Sebastien Leprince, Francois Ayoub, and Chris Milliner for helpful discussions and technical assistance. ASTER GDEM is a product of METI and NASA.

### References

- Ader, T., et al. (2012), Convergence rate across the Nepal Himalaya and interseismic coupling on the Main Himalayan Thrust: Implications for seismic hazard, *J. Geophys. Res.*, *117*, B04403, doi:10.1029/2011JB009071.
- Akyuz, H. S., R. Hartleb, A. Barka, E. Altunel, G. Sunal, B. Meyer, and R. Armijo (2002), Surface rupture and slip distribution of the 12 November 1999 Duzce earthquake (M 7.1), North Anatolian fault, Bolu, Turkey, *Bull. Seismol. Soc. Am.*, *92*(1), 61–66, doi:10.1785/0120000840.
- Ambraseys, N., and R. Bilham (2003), Earthquakes and associated deformation in northern Baluchistan 1892–2001, *Bull. Seismol. Soc. Am.*, *93*(4), 1573–1605, doi:10.1785/0120020038.
- Avouac, J. P., F. Ayoub, S. J. Wei, J. P. Ampuero, L. S. Meng, S. Leprince, R. Jolivet, Z. Duputel, and D. Helmberger (2014), The 2013, Mw 7.7 Balochistan earthquake, energetic strike-slip reactivation of a thrust fault, *Earth Planet. Sci. Lett.*, *391*, 128–134, doi:10.1016/j.epsl.2014.01.036.
- Ayoub, F., S. Leprince, and J. P. Avouac (2009a), Co-registration and correlation of aerial photographs for ground deformation measurements, *ISPRS J. Photogramm.*, *64*(6), 551–560, doi:10.1016/j.isprsjprs.2009.03.005.
- DigitalGlobe (2014), *DigitalGlobe: Content Collection*, Copyright 2014 DigitalGlobe, Inc. [Available at <http://www.digitalglobe.com/about-us/content-collection>, last accessed 4 Aug 2014]
- Dolan, J. F., and B. Haravitch (2014), How well do surface slip measurements track slip at depth in large strike-slip earthquakes? The importance of fault structural maturity in controlling on-fault slip versus off-fault surface deformation, *Earth Planet. Sci. Lett.*, *388*, 38–47, doi:10.1016/j.epsl.2013.11.043.
- Duffy, B., M. Quigley, D. J. A. Barrell, R. Van Dissen, T. Stahl, S. Leprince, C. McInnes, and E. Bilderback (2013), Fault kinematics and surface deformation across a releasing bend during the 2010 M-W 7.1 Darfield, New Zealand, earthquake revealed by differential LiDAR and cadastral surveying, *Geol. Soc. Am. Bull.*, *125*(3–4), 420–431, doi:10.1130/B30753.1.
- Duman, T. Y., Y. Awata, T. Yoshikazu, Ö. Emre, A. Dogan, and S. Özalp (2003), Surface rupture associated with the August 17, 1999 Izmit earthquake, in *Appendix 1 (Surface Rupture Maps and Slip Measurements)*, *Spec. Publ. Ser. 1*, edited by Ö. Emre, Y. Awata, and T. Y. Duman, pp. 57–86, Gen. Dir. of Minear Res. and Explor. (Maden Tetkik ve Arma Genel Müdürlüğü [MTA]), Ankara, Turkey.
- Elliott, J. R., E. K. Nissen, P. C. England, J. A. Jackson, S. Lamb, Z. Li, M. Oehlers, and B. Parsons (2012), Slip in the 2010–2011 Canterbury earthquakes, New Zealand, *J. Geophys. Res.*, *117*, B03401, doi:10.1029/2011JB008868.
- Fialko, Y., D. Sandwell, M. Simons, and P. Rosen (2005), Three-dimensional deformation caused by the Bam, Iran, earthquake and the origin of shallow slip deficit, *Nature*, *435*(7040), 295–299, doi:10.1038/nature03425.
- Google Earth (2013), Older alluvial fans, old alluvium, and bedrock along the Hoshab fault, Balochistan, Pakistan. 27°00'10" N, 65°26'30" E, Eye alt 5.76 km, V 7.1.2.2041, Copyright DigitalGlobe 2014. [Available at <http://www.earth.google.com>, last accessed 4 Aug 2014.]
- Google Earth (2014), Sediments and bedrock along the Hoshab fault, Balochistan, Pakistan. 26°24'45" N, 64°52'40"E, Eye alt 5.32 km, V 7.1.2.2041, Copyright DigitalGlobe 2014. [Available at <http://www.earth.google.com>, last accessed 4 Aug 2014.]
- Haeussler, P. J., et al. (2004a), Surface rupture and slip distribution of the Denali and Totschunda faults in the 3 November 2002 M 7.9 earthquake, Alaska, *Bull. Seismol. Soc. Am.*, *94*(6), 523–552, doi:10.1785/0120040626.
- Haeussler, P. J., D. P. Schwartz, T. E. Dawson, H. A. Stenner, J. J. Lienkaemper, F. Cinti, P. Montone, B. Sherrod, and P. Craw (2004b), Surface rupture of the 2002 Denali fault, Alaska, earthquake and comparison with other strike-slip ruptures, *Earth Spectra*, *20*(3), 565–578, doi:10.1193/1.1775797.
- Hartleb, R. D., et al. (2002), Surface rupture and slip distribution along the Karadere segment of the 17 August 1999 Izmit and the western section of the 12 November 1999 Duzce, Turkey, earthquakes, *Bull. Seismol. Soc. Am.*, *92*(1), 67–78, doi:10.1785/0120000829.
- Jolivet, R., et al. (2014), The 2013 M-w 7.7 Balochistan Earthquake: Seismic potential of an accretionary wedge, *Bull. Seismol. Soc. Am.*, *104*(2), 1020–1030, doi:10.1785/0120130313.
- Kaneko, Y., and Y. Fialko (2011), Shallow slip deficit due to large strike-slip earthquakes in dynamic rupture simulations with elasto-plastic off-fault response, *Geophys. J. Int.*, *186*(3), 1389–1403, doi:10.1111/j.1365-246X.2011.05117.x.
- Klinger, Y., X. W. Xu, P. Tapponnier, J. Van der Woerd, C. Lasserre, and G. King (2005), High-resolution satellite imagery mapping of the surface rupture and slip distribution of the M-W similar to 7.8, 14 November 2001 Kokoxili Earthquake, Kunlun Fault, northern Tibet, China, *Bull. Seismol. Soc. Am.*, *95*(5), 1970–1987, doi:10.1785/0120040233.
- Lawrence, R. D., S. H. Khan, K. A. Dejong, A. Farah, and R. S. Yeats (1981), Thrust and strike slip fault interaction along the Chaman transform zone, Pakistan, *Spec. Publ. Geol. Soc. London*, *9*, 363–370, doi:10.1144/GSL.SP.1981.009.01.33.
- Leprince, S., F. Ayoub, Y. Klinger, and J.-P. Avouac (2007a), Co-registration of optically sensed images and correlation (COSI-Corr): An operational methodology for ground deformation measurements, in *International Geoscience and Remote Sensing Symposium (IGARSS)*, vol. 6, pp. 2700–2702, IEEE Int., Barcelona, Spain.
- Leprince, S., S. Barbot, F. Ayoub, and J.-P. Avouac (2007b), Orthorectification, coregistration, and subpixel correlation of satellite images, application to ground deformation measurements, *IEEE Trans. Geosci. Remote Sens.*, *45*(6), 1529–1558.
- Leprince, S., P. Muse, and J. P. Avouac (2008), In-flight CCD distortion calibration for pushbroom satellites based on subpixel correlation, *IEEE Trans. Geosci. Remote Sens.*, *46*(9), 2675–2683, doi:10.1109/Tgrs.2008.918649.
- Liu, J., K. Sieh, and E. Hauksson (2003), A structural interpretation of the aftershock “Cloud” of the 1992 M-w 7.3 Landers earthquake, *Bull. Seismol. Soc. Am.*, *93*(3), 1333–1344, doi:10.1785/0120020060.
- Ma, S. (2008), A physical model for widespread near-surface and fault zone damage induced by earthquakes, *Geochem. Geophys. Geosyst.*, *9*, Q11009, doi:10.1029/2008GC002231.
- Ma, S., and D. J. Andrews (2010), Inelastic off-fault response and three-dimensional dynamics of earthquake rupture on a strike-slip fault, *J. Geophys. Res.*, *115*, B04304, doi:10.1029/2009JB006382.
- Milliner, C. W., J. F. Dolan, J. Hollingsworth, S. Leprince, and F. Ayoub (2014), Development of a standardized methodology for the use of COSI-Corr sub-pixel image correlation to determine surface deformation patterns in large magnitude earthquakes, Abstract T13C-4679 presented at 2014 Fall Meeting, AGU, San Francisco, Calif., 15–19 Dec.

- Mohadjer, S., et al. (2010), Partitioning of India-Eurasia convergence in the Pamir-Hindu Kush from GPS measurements, *Geophys. Res. Lett.*, 37, L04305, doi:10.1029/2009GL041737.
- Oskin, M. E., et al. (2012), Near-field deformation from the El Mayor-Cucapah Earthquake revealed by differential LIDAR, *Science*, 335(6069), 702–705, doi:10.1126/science.1213778.
- Platt, J. P., J. K. Leggett, and S. Alam (1988), Slip vectors and fault mechanics in the Makran accretionary wedge, Southwest Pakistan, *J. Geophys. Res.*, 93(B7), 7955–7973, doi:10.1029/Jb093ib07p07955.
- Reilinger, R., et al. (2006), GPS constraints on continental deformation in the Africa-Arabia-Eurasia continental collision zone and implications for the dynamics of plate interactions, *J. Geophys. Res.*, 111, B05411, doi:10.1029/2005JB004051.
- Rockwell, T. K., S. Lindvall, T. Dawson, R. Langridge, W. Lettis, and Y. Klinger (2002), Lateral offsets on surveyed cultural features resulting from the 1999 Izmit and Duzce earthquakes, Turkey, *Bull. Seismol. Soc. Am.*, 92(1), 79–94, doi:10.1785/0120000809.
- Shelef, E., and M. Oskin (2010), Deformation processes adjacent to active faults: Examples from eastern California, *J. Geophys. Res.*, 115, B05308, doi:10.1029/2009JB006289.
- Stirling, M. W., S. G. Wesnousky, and K. Shimazaki (1996), Fault trace complexity, cumulative slip, and the shape of the magnitude-frequency distribution for strike-slip faults: A global survey, *Geophys. J. Int.*, 124, 833–868.
- Sudhaus, H., and S. Jonsson (2011), Source model for the 1997 Zirkuh earthquake (M-W=7.2) in Iran derived from JERS and ERS InSAR observations, *Geophys. J. Int.*, 185(2), 676–692, doi:10.1111/j.1365-246X.2011.04973.x.
- Szeliga, W., R. Bilham, D. M. Kakar, and S. H. Lodi (2012), Interseismic strain accumulation along the western boundary of the Indian subcontinent, *J. Geophys. Res.*, 117, B08404, doi:10.1029/2011JB008822.
- Tong, X. P., D. T. Sandwell, and Y. Fialko (2010), Coseismic slip model of the 2008 Wenchuan earthquake derived from joint inversion of interferometric synthetic aperture radar, GPS, and field data, *J. Geophys. Res.*, 115, B04314, doi:10.1029/2009JB006625.
- Treiman, J. A., K. J. Kendrick, W. A. Bryant, T. K. Rockwell, and S. F. McGill (2002), Primary surface rupture associated with the M-w 7.1 16 October 1999 Hector Mine earthquake, San Bernardino County, California, *Bull. Seismol. Soc. Am.*, 92(4), 1171–1191, doi:10.1785/0120000923.
- U.S. Department of the Interior, U.S. Geological Survey (2013), M7.7 – 61 km NNE of Awaran, Pakistan (BETA). [Available at <http://comcat.cr.usgs.gov/earthquakes/eventpage/usb000jyiv>, last accessed 4 Aug 2014]
- Van Dissen, R., et al. (2011), Surface rupture displacement on the Greendale Fault during the M (sub w) 7.1 Darfield (Canterbury) earthquake, New Zealand, and its impact on man-made structures, in *Proceedings Ninth Pacific Conference on Earthquake Engineering, Building an Earthquake-Resilient Society*, Pap. 186, 8 pp, N. Z. Soc. for Earthquake Eng., Auckland, 14–16 April 2011.
- Wei, S. J., et al. (2011), Superficial simplicity of the 2010 El Mayor-Cucapah earthquake of Baja California in Mexico, *Nat. Geosci.*, 4(9), 615–618, doi:10.1038/Ngeo1213.
- Wesnousky, S. G. (1988), Seismological and structural evolution of strike-slip faults, *Nature*, 335(6188), 340–342, doi:10.1038/335340a0.
- Xu, X. W., G. H. Yu, Y. Klinger, P. Tapponnier, and J. Van der Woerd (2006), Reevaluation of surface rupture parameters and faulting segmentation of the 2001 Kunlunshan earthquake (M(w)7.8), northern Tibetan Plateau, China, *J. Geophys. Res.*, 111, B05316, doi:10.1029/2004JB003488.